



Cite this: *Phys. Chem. Chem. Phys.*,  
2018, 20, 22909

# Low-temperature activation of methane on doped single atoms: descriptor and prediction†

Victor Fung,<sup>a</sup> Franklin (Feng) Tao<sup>b\*</sup> and De-en Jiang<sup>b\*†</sup>

Catalytic transformation of methane under mild conditions remains a grand challenge. Fundamental understanding of C–H activation of methane is crucial for designing a catalyst for the utilization of methane at low temperature. Recent experiments show that strong methane chemisorption on oxides of precious metals leads to facile C–H activation. However, only a very few such oxides are capable (for example, IrO<sub>2</sub> and PdO). Here we show for the first time that strong methane chemisorption and facile C–H activation can be accomplished by single transition-metal atoms on TiO<sub>2</sub>, some of which are even better than IrO<sub>2</sub>. Using methane adsorption energy as a descriptor, we screened over 30 transition-metal single atoms doped on TiO<sub>2</sub> for the chemisorption of methane by replacing a surface Ti atom with a single atom of another transition metal. It is found that the adsorption energies of methane on a single atom of Pd, Rh, Os, Ir, and Pt doped on rutile TiO<sub>2</sub>(110) are greater than or similar to those on rutile IrO<sub>2</sub>(110), a benchmark for the chemisorption of methane on transition oxides. Electronic structure analysis uncovered orbital overlap and mixing between methane and the single atom, as well as significant localization of the charge between the molecule and the surface, demonstrating chemical bonding of CH<sub>4</sub> to doped single atoms. Facile C–H dissociation has been found on the single-atom sites with the transition state energies lower than desorption energies. Our computational studies predict that Pd, Rh, Os, Ir, and Pt single atoms on rutile TiO<sub>2</sub>(110) can activate C–H of methane at a temperature lower than 25 °C.

Received 18th May 2018,  
Accepted 10th August 2018

DOI: 10.1039/c8cp03191f

rsc.li/pccp

## 1. Introduction

Methane is an inexpensive energy resource. Hydraulic fracturing that supplies much of the earth-abundant source from shale is of particular economic and scientific significance.<sup>1–3</sup> The existing catalytic processes in industry to convert methane to fuel or chemicals employ mainly partial oxidation by O<sub>2</sub> and reforming through CO<sub>2</sub> or H<sub>2</sub>O, which are performed at high temperatures. From a thermodynamic point of view, it is feasible to activate methane and transform it to a chemical and fuel feedstock at a relatively low temperature (<200 °C). A kinetically favorable activation of C–H of methane is important for the realization of the catalytic transformation of methane at a relatively low temperature. Hutchings *et al.* have pioneered the experimental exploration of anchored cations in zeolites and demonstrated the

activation of C–H on Cu and Fe anchored in microporous aluminosilicate.<sup>4,5</sup>

Transition metal oxides have been extensively explored for catalytic methane conversion. There are two primary pathways for the cleavage of the C–H bond on metal oxides:<sup>6–9</sup> the heterolytic pathway by which the C–H bond is cleaved over a metal–oxygen pair and methyl is stabilized on a metal site; the homolytic pathway by which the C–H bond is cleaved directly over a surface oxygen to form a radical-like intermediate.<sup>10,11</sup> The homolytic H abstraction pathway is predicted to occur with lower barriers for redox-facile oxides,<sup>7,12</sup> consistent with density functional theory (DFT) calculations.<sup>13–16</sup> Furthermore, the use of easily computable quantities such as lattice oxygen coordination<sup>17</sup> and hydrogen adsorption energy<sup>17–20</sup> as descriptors enables quick screening of metal-oxide active sites for the best homolytic C–H activation ability.

Instead of the homolytic cleavage which usually occurs at high temperature, the heterolytic pathway has recently gained interest in the chemisorption and low-temperature activation of methane. Ni and Co supported on CeO<sub>2</sub><sup>21–23</sup> have been demonstrated to be promising methane activation and dry reforming catalysts *via* the low C–H activation barriers from a chemisorbed methane complex. Weaver *et al.* reported the first case of experimentally observed low-temperature methane C–H activation on rutile IrO<sub>2</sub> at 150 K,<sup>24</sup> supported by earlier DFT calculations

<sup>a</sup> Department of Chemistry, University of California, Riverside, CA 92521, USA.  
E-mail: djiang@ucr.edu

<sup>b</sup> Department of Chemical and Petroleum Engineering and Department of Chemistry, University of Kansas, Lawrence, KS 66045, USA.  
E-mail: franklin.feng.tao@ku.edu

† Electronic supplementary information (ESI) available: Structure models; analysis of methane adsorption and electronic structure; correlations of bond distance and C–H activation energy; tables of key energetics and geometry; and a test of different DFT functionals. See DOI: 10.1039/c8cp03191f

showing methane chemisorption and a lower activation energy for surface C–H dissociation than methane desorption.<sup>25</sup>

Single-atom catalysts have attracted great attention recently and can be potentially useful for methane activation. They usually comprise noble-metal single atoms on an oxide support.<sup>26–28</sup> TiO<sub>2</sub> has been used as a support to anchor single atoms and played a significant role in single atom catalysis, particularly in photocatalysis and CO oxidation.<sup>29–32</sup> Unmodified TiO<sub>2</sub> is not active for methane activation, and methane only weakly interacts with it.<sup>33</sup> Surface doping of guest cations could dramatically change the electronic state of the guest cations since doping typically provides a different chemical and coordination environment for the guest cations.<sup>19,34–37</sup> Depending on the dopant and the synthesis method, the dopant may prefer to be situated in the cationic vacancies.<sup>26,38–40</sup>

The capability of IrO<sub>2</sub> to activate methane at low temperatures and the idea of using single-atom catalysts for methane activation inspired us to propose the use of methane adsorption energy as a descriptor to screen single-atom systems that have similar local surface structures to IrO<sub>2</sub>. To this end, we use first principles density functional theory to test all d-block single atoms substitutionally situated in a common oxide support, TiO<sub>2</sub> (especially the rutile phase in the analogue to IrO<sub>2</sub>), and then examine and analyze their propensity for methane adsorption and dissociation.

## 2. Methods

Density functional theory (DFT) calculations were performed using the Vienna ab initio Simulation Package (VASP).<sup>41,42</sup> The on-site Coulomb interaction was included with the DFT+*U* method by Dudarev, *et al.*<sup>43</sup> in the VASP using a Hubbard parameter  $U = 3$  eV for the Ti atom, as demonstrated to perform well in previous studies of TiO<sub>2</sub>.<sup>44,45</sup> The Perdew–Burke–Ernzerhof (PBE)<sup>46</sup> functional form of the generalized-gradient approximation (GGA) was used for electron exchange and correlation energies. Additional validation at the PBE-D3, SCAN, and HSE06 levels was also performed as described in the main text. All calculations were performed with spin polarization. The projector-augmented wave method was used to describe the electron–core interaction.<sup>41,47</sup> A kinetic energy cutoff of 450 eV was used for the plane waves. The Brillouin zone was sampled with the Monkhorst–Pack scheme of a  $3 \times 2 \times 1$  *k*-point mesh.<sup>48</sup> A vacuum layer of 15 Å was added for the surface slabs along the *z*-direction; the slabs contain a total of four layers, with the bottom two layers fixed in their bulk positions.

The methane adsorption energy ( $E_{\text{ads}}$ ) is calculated with the equation  $E_{\text{ads}} = E_{\text{surface+CH}_4} - (E_{\text{perfect-surface}} + E_{\text{CH}_4})$ , where  $E_{\text{surface+CH}_4}$  is the energy of the surface slab with a methane. The energy  $E_{\text{CH}_4}$  was computed by placing the adsorbate in a cubic cell with a 15 Å wide vacuum in each direction. Transition states (TSs) were found with the nudged elastic band (NEB)<sup>49</sup> and the dimer method<sup>50</sup> implemented in the VASP-VTST package using a force convergence criterion of 0.05 eV Å<sup>-1</sup>. To compute the free energy for the profile of methane activation on Pt–TiO<sub>2</sub>, the zero-point energy (ZPE) and entropy of the adsorbed species were obtained from DFT vibrational frequencies, while the JANAF tables

were referenced for gas phase methane. The change in ZPE of Pt–TiO<sub>2</sub> for adsorption was found to be less than 0.04 eV and omitted for the other screened elements. Charge densities and isosurfaces were visualized using the VESTA program.<sup>51</sup>

To calculate the occupancies of the molecular bonds of methane, the periodic natural bond orbital (NBO) analysis implemented by Schmidt *et al.* was used.<sup>52</sup> The plane wave basis from the VASP is projected onto def2-SVP basis sets.<sup>53</sup> To avoid numerical instabilities due to diffuse orbitals in the Gaussian basis sets,<sup>54</sup> orbitals with exponents lower than 0.1 were simply truncated for the metals; despite this, the atomic orbitals of the methane molecule remained well represented.

## 3. Results and discussion

### 3.1 Geometry and energies of chemisorbed methane on M–TiO<sub>2</sub>

We chose TiO<sub>2</sub> anatase(101) and rutile(110), the two most commonly studied facets of TiO<sub>2</sub>, to study the effect of single-atom sites on methane adsorption. First, the popular DFT-PBE method was used, while validation with more advanced functionals will be discussed later. On both surfaces, the surface single-atom or M<sub>1</sub> site is coordinated to four surface oxygens and one subsurface oxygen. The binding energies for selected dopants to the Ti vacancy can be found in Table S1 (ESI<sup>†</sup>), which are lower in energy than for adsorption in the O vacancy and on top of the pristine surface (Fig. S1, ESI<sup>†</sup>). Furthermore, the diffusion of the metal dopant out of the cationic vacancy shows high barriers and is endothermic in energy (Fig. S2, ESI<sup>†</sup>). We screened single atoms of all transition metal elements doped on TiO<sub>2</sub> and found that methane adsorption is stronger on the single-atom site on the rutile(110) surface than on the anatase(101) surface (see Fig. S3 and Table S2 in the ESI<sup>†</sup> for the comparison). More importantly, we have identified guest metal elements whose cations exhibit strong chemisorption of methane on M<sub>1</sub>–rutile-TiO<sub>2</sub>(110) systems, which is the focus of the present work. Fig. 1 shows the local coordination of the M<sub>1</sub>–rutile-TiO<sub>2</sub>(110) system and a typical

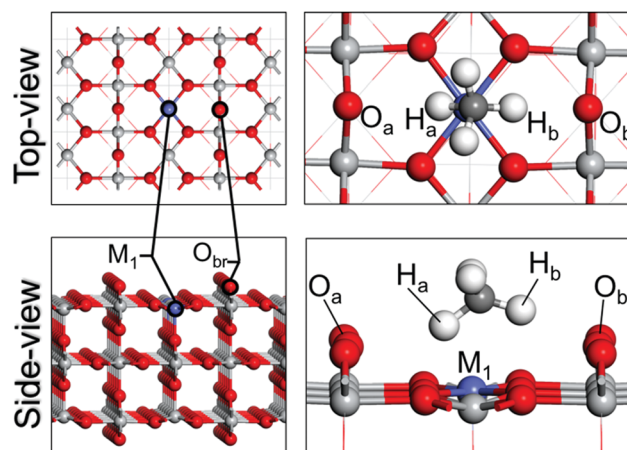


Fig. 1 Structural representations of the single-atom site, M<sub>1</sub> (blue), doped on the rutile TiO<sub>2</sub>(110) surface (left) and CH<sub>4</sub> adsorption on the site (right). Ti, grey; O, red; C, dark grey; H, white.

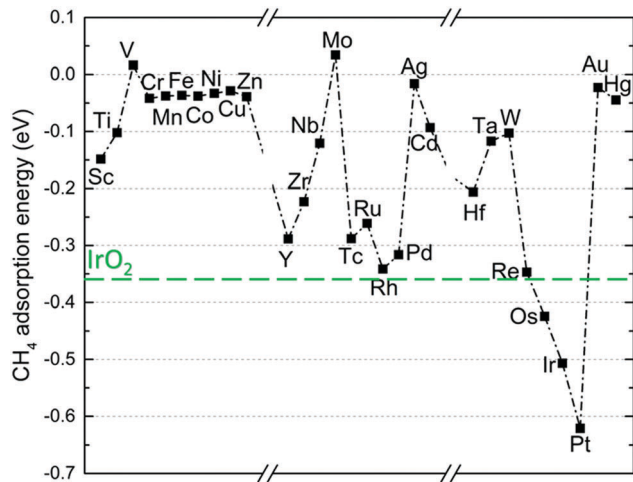


Fig. 2 Adsorption energies of methane on the  $M_1$  (single-atom) site on rutile  $\text{TiO}_2(110)$  with  $M$  being 3d, 4d, and 5d transition metals, in comparison with that on rutile  $\text{IrO}_2(110)$  (green line). The Ti datum represents the undoped rutile  $\text{TiO}_2(110)$ .

geometry of a chemisorbed  $\text{CH}_4$  on it. One can see that  $\text{CH}_4$  is located above the single atom ( $M_1$ ) and between two bridging oxygen sites ( $O_a$  and  $O_b$ ). The molecule slightly tilts on one side, with one H atom pointing more downwards (denoted as  $H_a$ ).

Fig. 2 shows the adsorption energy of  $\text{CH}_4$  for all the d-block transition metal single atoms on the rutile  $\text{TiO}_2(110)$  surface (a heatmap on the periodic table is provided in Fig. S4 and the values are given in Table S3, ESI<sup>†</sup>). One can see that 3d metals all have weak  $\text{CH}_4$  adsorption, because their d orbitals are too contracted; among the 4d metals, Pd and Rh have the strongest adsorption; among the 5d metals, Re, Os, Ir, and Pt have higher adsorption energies than Pd and Rh. If one uses methane adsorption on rutile  $\text{IrO}_2(110)$  as a benchmark ( $-0.36$  eV; green line in Fig. 2), one can see that Os, Ir and Pt single atoms on rutile  $\text{TiO}_2(110)$  have even stronger  $\text{CH}_4$  adsorption. Especially,  $\text{Pt}_1$ -rutile- $\text{TiO}_2(110)$ , shortened as  $\text{Pt}_1$ - $\text{TiO}_2$  below, is predicted to have an adsorption energy of  $-0.62$  eV at the DFT-PBE level, the strongest methane adsorption on an undecorated solid surface reported to date.<sup>55,56</sup> For comparison, the  $\text{CH}_4$  adsorption energy is  $-0.10$  eV on the Ti site of the perfect rutile  $\text{TiO}_2(110)$  surface, while  $\text{CH}_4$  adsorption on isolated gas-phase single atoms is also weak (Table S4, ESI<sup>†</sup>;  $E_{\text{ad}}$  ranging from  $-0.01$  to  $-0.23$  eV). It is evident that the coordination to the rutile  $\text{TiO}_2$  surface has modified the electronic structure of the single-atom site for chemisorption. Below we analyze in-depth how  $\text{CH}_4$  interacts with the  $\text{Pt}_1$ - $\text{TiO}_2$  surface chemically.

### 3.2 Electronic structure of the methane $\sigma$ complex

Chemisorption of methane is hypothesized to involve the formation of an alkane  $\sigma$  complex.<sup>56–58</sup> Fig. 3A and B shows the electronic-density-difference plots for  $\text{CH}_4$  adsorption on  $\text{Pt}_1$ - $\text{TiO}_2$ . The transfer of electron density from the C–H bonds and the Pt atom to the region between the C– $H_a$  bond and Pt is clearly seen. The charge depletion on Pt is likely the result of the back-bonding into  $\text{CH}_4$  antibonding orbitals. Slight charge accumulation is

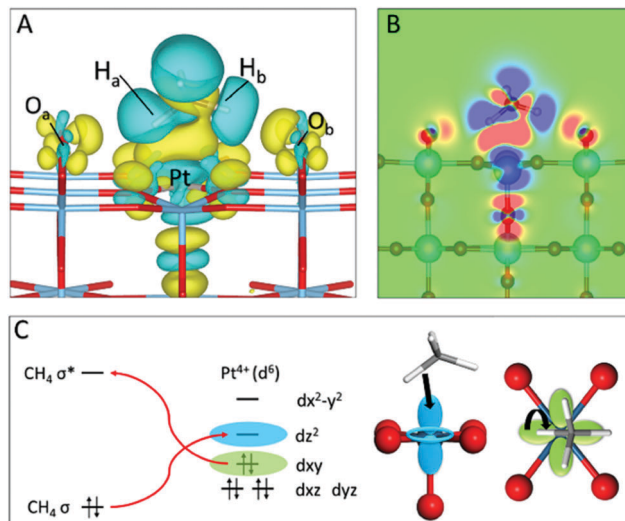


Fig. 3 (A) Isosurface plot of the charge density difference from  $\text{CH}_4$  adsorption on  $\text{Pt}_1$ -rutile- $\text{TiO}_2(110)$ : yellow, charge accumulation; cyan, charge depletion. (B) 2-D charge density plot on the  $H_a$ -C- $H_b$  plane: red, charge accumulation; blue, charge depletion. (C) Schematic of orbital interactions between  $\text{CH}_4$  and  $\text{Pt}^{4+}$ .

found on  $O_a$  and  $O_b$ , due to the hydrogen-bond interaction between the C–H and O, which is made possible by the significant polarization of the C–H bond and the loss of charge density on  $H_a$  and  $H_b$ . Bader charge analysis shows a net increase in electron density on the carbon and a net decrease in electron density on  $H_b$  and  $H_a$  (Table S5, ESI<sup>†</sup>), with a slight net loss of electron density on  $\text{CH}_4$ . A similar charge-transfer pattern is also found for  $\text{CH}_4$  adsorption on  $\text{Ir}_1$ - $\text{TiO}_2$  (Fig. S5 and S6, ESI<sup>†</sup>). The local density-of-states plots (Fig. S7, ESI<sup>†</sup>) show mixing of  $\text{CH}_4$  orbitals and dopant d states. More specifically, the electron donation occurs from the C–H bond to the metal  $d_{z^2}$  orbital, and back-donation occurs from the metal  $d_{xy}$  orbital to the C–H  $\sigma^*$  orbital, as illustrated in a schematic (Fig. 3C) using the  $d^6$  configuration of  $\text{Pt}^{4+}$ . Less or more d electrons (Fig. S8, ESI<sup>†</sup>) lead to weakened interaction with  $\text{CH}_4$ .

To reveal the extent of the weakening of the C– $H_a$  bond, we used the natural bond orbital (NBO) analysis to determine the effective  $\sigma$  occupancy, *i.e.*, the difference in occupancy between  $\sigma$  and  $\sigma^*$ .<sup>54</sup> Fig. 4 shows a linear correlation between C– $H_a$   $\sigma$ - $\sigma^*$  occupancy and  $\text{CH}_4$  adsorption energy, confirming that the greatest weakening of the C– $H_a$  bond takes place on  $\text{Pt}_1$ - $\text{TiO}_2$  as suggested by the chemisorption model in Fig. 3C. The weakening of the C– $H_a$  bond and the polarization of the  $\text{CH}_4$  molecule are further reflected in the linear correlations of the C– $H_a$  bond length and the C–M (single atom) distance with  $\text{CH}_4$  adsorption energy (Fig. S9, ESI<sup>†</sup>).

### 3.3 Methane C–H activation barriers and linear scaling descriptors

For single-atom sites yielding the strongest chemisorption of  $\text{CH}_4$ , the heterolytic C–H activation on them are expected to be facile as well. We have located transition states of the heterolytic C–H activation for these single-atom sites on rutile  $\text{TiO}_2(110)$ .

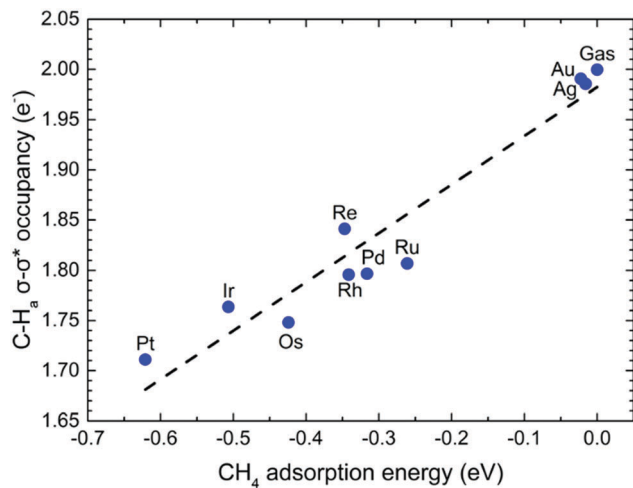


Fig. 4 Linear correlation between methane C-H<sub>a</sub>  $\sigma$ - $\sigma^*$  occupancy and adsorption energy on the M<sub>1</sub> (single-atom) site on rutile TiO<sub>2</sub>(110) with M being various transition metals.

Of all the single atoms, Pt<sub>1</sub> and Pd<sub>1</sub> have the lowest methane dissociation barriers of only 0.15 and 0.13 eV, respectively. Fig. 5 illustrates the minimum free-energy path for CH<sub>4</sub> dissociation on Pt<sub>1</sub>-TiO<sub>2</sub>, characterized by the lengthening of the C-H<sub>a</sub> bond and the shortening of the C-Pt distance, which eventually results in a hydroxyl group on the O<sub>a</sub> site and a methyl group coordinated to Pt. One can see from Fig. 5 that facile C-H activation is predicted on Pt<sub>1</sub>-TiO<sub>2</sub> below room temperature instead of desorption, due to the strong adsorption of CH<sub>4</sub>.

We further explored methane dissociation on other single atoms on rutile TiO<sub>2</sub>(110). Interestingly, we found that the first C-H activation energy and dissociation energy of CH<sub>4</sub> on the chemisorbing surface sites (blue circles in Fig. 6A) follow the

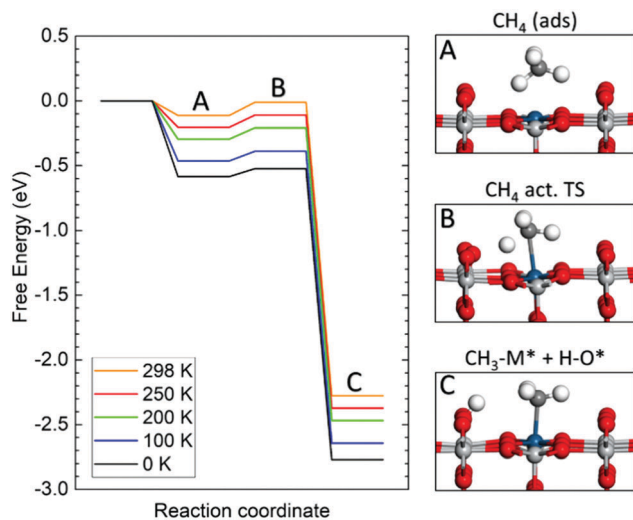


Fig. 5 Free energy profile of CH<sub>4</sub> activation on Pt<sub>1</sub>-rutile-TiO<sub>2</sub>(110) for a range of temperatures from 0 to 298 K. The structures for the initial state (A), transition state (B), and final state (C) are shown on the right. The free energies are obtained by including the zero point and vibrational contributions. The vibrational frequencies are obtained from the DFT calculations.

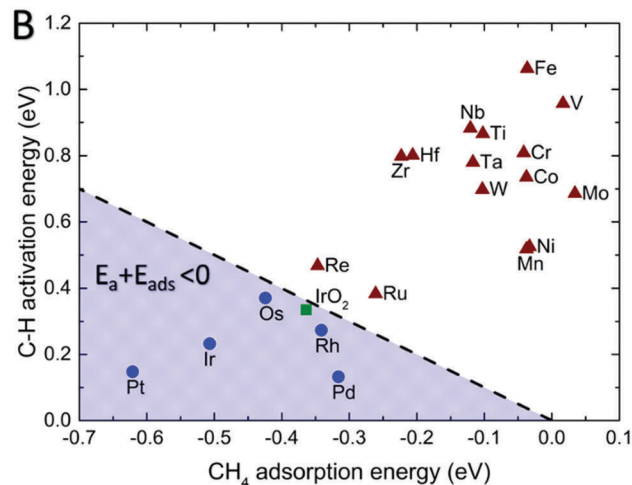
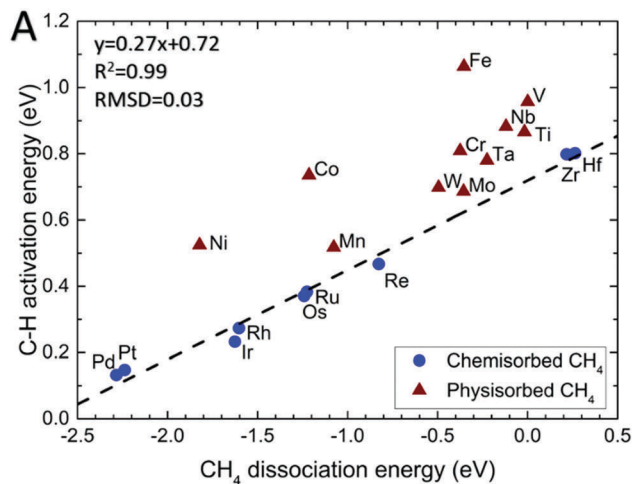


Fig. 6 (A) Correlation between C-H activation energy ( $E_a$ ) and dissociation energy ( $\Delta E$ ) of CH<sub>4</sub> on the M<sub>1</sub> site on rutile TiO<sub>2</sub>(110) with M being various transition metals. A linear correlation plot is drawn for the chemisorbing dopants (blue circles) and fitting parameters shown in the top left. (B) C-H activation energy ( $E_a$ ) vs. adsorption energy of CH<sub>4</sub> ( $E_{ads}$ ) on the M<sub>1</sub> site on rutile TiO<sub>2</sub>(110) with M being various transition metals, in comparison with rutile IrO<sub>2</sub>(110); in the shaded region, low-temperature activation of CH<sub>4</sub> is most likely. The point labeled 'Ti' denotes the undoped TiO<sub>2</sub>(110) surface.

Bronsted-Evans-Polanyi (BEP) relationship ( $R^2 = 0.99$ ).<sup>59-61</sup> The BEP  $\alpha$  value is 0.27, suggesting an early transition state with a major influence of both the reactant chemisorption and the product (dissociation) energies. Furthermore, the obtained linear correlation for the methane-chemisorbing single atoms lies beneath physisorbing ones (brown triangles in Fig. 6A), suggesting the stabilizing and energy-lowering effect of chemisorption on transition state energies.

For low-temperature methane activation to occur, the energy of the transition state of C-H activation ( $E_a$ ) must be lower than the energy of desorption ( $E_d$ , the opposite of the adsorption energy  $E_{ads}$ ) of the reactant CH<sub>4</sub> molecule to the gas phase. The shaded area in Fig. 6B where  $E_a - E_d = E_a + E_{ads} < 0$  therefore denotes the region where the low-temperature activation is most likely. One can see that these include the Pd, Rh, Os, Ir, and Pt single atoms. The Re and Ru elements lie close to the

boundary and also possibly activate CH<sub>4</sub> at low temperature on rutile TiO<sub>2</sub>(110).

### 3.4 Validation and comparison of functionals

To be able to compare with previous works,<sup>24,25,56,62</sup> we have used the DFT-PBE functional to describe CH<sub>4</sub> adsorption and activation on M<sub>1</sub>-TiO<sub>2</sub> sites. To confirm our main findings above based on the GGA-PBE energies, further calculations were performed using PBE-D3 to include dispersion interaction,<sup>63</sup> a recent meta-GGA (SCAN<sup>64</sup>), a hybrid functional (HSE06),<sup>65</sup> and a van der Waals density functional (optPBE-vdW).<sup>66</sup> As shown in Table S6 (ESI<sup>†</sup>), the different functionals give slight variations in CH<sub>4</sub> adsorption energies and the transition state energies. Despite these variations, the main conclusions remain the same in all cases that the single-atom sites such as Ir and Pt on rutile TiO<sub>2</sub>(110) are most promising for low temperature CH<sub>4</sub> activation, due to strong CH<sub>4</sub> chemisorption and low C-H activation energy.

### 3.5 Implications

Our results above indicate that CH<sub>4</sub> activation on a site such as on Pt<sub>1</sub>-TiO<sub>2</sub> would be facile. To our knowledge, there has been no experimental report on this, so we look forward to the experimental realization. After the first C-H activation step, one possible follow-up route is *via* the oxidative coupling process to form ethane and then ethylene. Fig. 5 suggests that the binding of CH<sub>3</sub> and H on Pt<sub>1</sub>-TiO<sub>2</sub> is strong, given the very negative energy change. This may impede subsequent reactions. But a recent DFT study on IrO<sub>2</sub> has shown that the coupling barriers can be very low despite similarly strong metal-CH<sub>x</sub> bonds.<sup>67</sup> We expect that a similar process can be catalyzed by Pt<sub>1</sub>-TiO<sub>2</sub>.

Methane chemisorption energy seems to be a good descriptor for identifying M<sub>1</sub>-TiO<sub>2</sub> sites that activate C-H facilely. We expect that this descriptor can be extended to other oxides and oxide-supported single-atom sites. In contrast, on pure metal surfaces, the descriptor used is generally the methane dissociation energy.<sup>68</sup>

## 4. Conclusions

In summary, we screened single atoms of all 3d, 4d, and 5d transition-metal elements doped on TiO<sub>2</sub> surfaces for the chemisorption of CH<sub>4</sub> and heterolytic C-H activation from first principles calculations. DFT-PBE identified the chemisorption of CH<sub>4</sub> and predicted that Rh, Pd, Os, Pt and Ir single atoms on rutile TiO<sub>2</sub>(110) would chemisorb CH<sub>4</sub> equally to or even stronger than on IrO<sub>2</sub>(110). Detailed electronic structure analysis and correlations show that CH<sub>4</sub> is polarized by the single atom's extended d orbitals through  $\sigma$ -complex formation as well as by the surface oxygen atoms on the rutile TiO<sub>2</sub>(110) surface. Further studies confirmed that CH<sub>4</sub> can be activated by these single-atom sites facilely from the chemisorption configuration following a heterolytic pathway. Our work suggests a very promising approach to realize low-temperature transformation of methane on precious metal single-atom sites doped on rutile TiO<sub>2</sub>. To our knowledge, this is the first time that such an M<sub>1</sub>-TiO<sub>2</sub> system has been predicted to activate CH<sub>4</sub> based on strong chemisorption.

## Conflicts of interest

The authors declare no competing financial interests.

## Acknowledgements

This research is sponsored by Chemical Sciences, Geosciences and Biosciences Division, Office of Basic Energy Sciences, Office of Science, U.S. Department of Energy, under Grant No. DE-SC0014561. This research used resources of the National Energy Research Scientific Computing Center, a DOE Office of Science User Facility supported by the Office of Science of the U.S. Department of Energy under Contract No. DE-AC02-05CH11231.

## References

- 1 P. Schwach, X. Pan and X. Bao, *Chem. Rev.*, 2017, **117**, 8497–8520.
- 2 R. Horn and R. Schlögl, *Catal. Lett.*, 2015, **145**, 23–39.
- 3 W. Taifan and J. Baltrusaitis, *Appl. Catal., B*, 2016, **198**, 525–547.
- 4 C. Hammond, M. M. Forde, A. Rahim, M. Hasbi, A. Thetford, Q. He, R. L. Jenkins, N. Dimitratos, J. A. Lopez-Sanchez and N. F. Dummer, *Angew. Chem., Int. Ed.*, 2012, **51**, 5129–5133.
- 5 M. M. Forde, R. D. Armstrong, C. Hammond, Q. He, R. L. Jenkins, S. A. Kondrat, N. Dimitratos, J. A. Lopez-Sanchez, S. H. Taylor, D. Willock, C. J. Kiely and G. J. Hutchings, *J. Am. Chem. Soc.*, 2013, **135**, 11087–11099.
- 6 J. K. Nørskov, F. Abild-Pedersen, F. Studt and T. Bligaard, *Proc. Natl. Acad. Sci. U. S. A.*, 2011, **108**, 937–943.
- 7 H. Schwarz, *Angew. Chem., Int. Ed.*, 2011, **50**, 10096–10115.
- 8 N. Dietl, M. Schlangen and H. Schwarz, *Angew. Chem., Int. Ed.*, 2012, **51**, 5544–5555.
- 9 F. F. Tao, J. J. Shan, L. Nguyen, Z. Wang, S. Zhang, L. Zhang, Z. Wu, W. Huang, S. Zeng and P. Hu, *Nat. Commun.*, 2015, **6**, 7798.
- 10 D. Hibbitts and M. Neurock, *Surf. Sci.*, 2016, **650**, 210–220.
- 11 B. Xing, X.-Y. Pang and G.-C. Wang, *J. Catal.*, 2011, **282**, 74–82.
- 12 J. H. Lunsford, *Angew. Chem., Int. Ed.*, 1995, **34**, 970–980.
- 13 V. Fung, F. F. Tao and D.-E. Jiang, *Catal. Sci. Technol.*, 2016, **6**, 6861–6869.
- 14 K. Kwapien, J. Paier, J. Sauer, M. Geske, U. Zavyalova, R. Horn, P. Schwach, A. Trunschke and R. Schlögl, *Angew. Chem., Int. Ed.*, 2014, **53**, 8774–8778.
- 15 H. Fu, Z.-P. Liu, Z.-H. Li, W.-N. Wang and K.-N. Fan, *J. Am. Chem. Soc.*, 2006, **128**, 11114–11123.
- 16 M. D. Krcha, A. D. Mayernick and M. J. Janik, *J. Catal.*, 2012, **293**, 103–115.
- 17 V. Fung, F. F. Tao and D. E. Jiang, *J. Phys. Chem. Lett.*, 2017, **8**, 2206–2211.
- 18 A. A. Latimer, A. R. Kulkarni, H. Aljama, J. H. Montoya, J. S. Yoo, C. Tsai, F. Abild-Pedersen, F. Studt and J. K. Nørskov, *Nat. Mater.*, 2017, **16**, 225–229.
- 19 G. Kumar, S. L. J. Lau, M. D. Krcha and M. J. Janik, *ACS Catal.*, 2016, **6**, 1812–1821.

- 20 P. Deshlahra and E. Iglesia, *J. Phys. Chem. C*, 2016, **120**, 16741–16760.
- 21 Z. Liu, D. C. Grinter, P. G. Lustemberg, T. D. Nguyen-Phan, Y. Zhou, S. Luo, I. Waluyo, E. J. Crumlin, D. J. Stacchiola and J. Zhou, *Angew. Chem., Int. Ed.*, 2016, **55**, 7455–7459.
- 22 Z. Liu, P. Lustemberg, R. A. Gutiérrez, J. J. Carey, R. M. Palomino, M. Vorokhta, D. C. Grinter, P. J. Ramírez, V. Matolín and M. Nolan, *Angew. Chem., Int. Ed.*, 2017, **56**, 13041–13046.
- 23 P. G. Lustemberg, P. J. Ramírez, Z. Liu, R. A. Gutierrez, D. G. Grinter, J. Carrasco, S. D. Senanayake, J. A. Rodriguez and M. V. Ganduglia-Pirovano, *ACS Catal.*, 2016, **6**, 8184–8191.
- 24 Z. Liang, T. Li, M. Kim, A. Asthagiri and J. F. Weaver, *Science*, 2017, **356**, 299–303.
- 25 C.-C. Wang, S. S. Siao and J.-C. Jiang, *J. Phys. Chem. C*, 2012, **116**, 6367–6370.
- 26 B. Qiao, A. Wang, X. Yang, L. F. Allard, Z. Jiang, Y. Cui, J. Liu, J. Li and T. Zhang, *Nat. Chem.*, 2011, **3**, 634–641.
- 27 L. Nie, D. Mei, H. Xiong, B. Peng, Z. Ren, X. I. P. Hernandez, A. DeLaRiva, M. Wang, M. H. Engelhard, L. Kovarik, A. K. Datye and Y. Wang, *Science*, 2017, **358**, 1419–1423.
- 28 L. DeRita, S. Dai, K. Lopez-Zepeda, N. Pham, G. W. Graham, X. Pan and P. Christopher, *J. Am. Chem. Soc.*, 2017, **139**, 14150–14165.
- 29 P. Liu, Y. Zhao, R. Qin, S. Mo, G. Chen, L. Gu, D. M. Chevrier, P. Zhang, Q. Guo, D. Zang, B. Wu, G. Fu and N. Zheng, *Science*, 2016, **352**, 797–801.
- 30 S. Li, X. Zhao, J. Shi, Y. Jia, Z. Guo, J.-H. Cho, Y. Gao and Z. Zhang, *Phys. Chem. Chem. Phys.*, 2016, **18**, 24872–24879.
- 31 J. Shi, X. Zhao, L. Zhang, X. Xue, Z. Guo, Y. Gao and S. Li, *J. Mater. Chem. A*, 2017, **5**, 19316–19322.
- 32 Y. Sui, S. Liu, T. Li, Q. Liu, T. Jiang, Y. Guo and J.-L. Luo, *J. Catal.*, 2017, **353**, 250–255.
- 33 L. Chen, R. S. Smith, B. D. Kay and Z. Dohnalek, *Surf. Sci.*, 2016, **650**, 83–92.
- 34 E. W. McFarland and H. Metiu, *Chem. Rev.*, 2013, **113**, 4391–4427.
- 35 B. Li and H. Metiu, *J. Phys. Chem. C*, 2010, **114**, 12234–12244.
- 36 X. Sun, B. Li and H. Metiu, *J. Phys. Chem. C*, 2013, **117**, 7114–7122.
- 37 V. Fung, F. F. Tao and D.-E. Jiang, *ChemCatChem*, 2018, **10**, 244–249.
- 38 J. Zhang, X. Wu, W.-C. Cheong, W. Chen, R. Lin, J. Li, L. Zheng, W. Yan, L. Gu, C. Chen, Q. Peng, D. Wang and Y. Li, *Nat. Chem.*, 2018, **9**, 1002.
- 39 R. Bliem, J. Pavelec, O. Gamba, E. McDermott, Z. Wang, S. Gerhold, M. Wagner, J. Osiecki, K. Schulte, M. Schmid, P. Blaha, U. Diebold and G. S. Parkinson, *Phys. Rev. B: Condens. Matter Mater. Phys.*, 2015, **92**, 075440.
- 40 B. Qiao, J. Liu, Y.-G. Wang, Q. Lin, X. Liu, A. Wang, J. Li, T. Zhang and J. Liu, *ACS Catal.*, 2015, **5**, 6249–6254.
- 41 G. Kresse and J. Furthmuller, *Comput. Mater. Sci.*, 1996, **6**, 15–50.
- 42 G. Kresse and J. Furthmuller, *Phys. Rev. B: Condens. Matter Mater. Phys.*, 1996, **54**, 11169–11186.
- 43 S. L. Dudarev, G. A. Botton, S. Y. Savrasov, C. J. Humphreys and A. P. Sutton, *Phys. Rev. B: Condens. Matter Mater. Phys.*, 1998, **57**, 1505–1509.
- 44 Z. Hu and H. Metiu, *J. Phys. Chem. C*, 2011, **115**, 5841–5845.
- 45 E. Finazzi, C. Di Valentin, G. Pacchioni and A. Selloni, *J. Chem. Phys.*, 2008, **129**, 154113.
- 46 J. P. Perdew, K. Burke and M. Ernzerhof, *Phys. Rev. Lett.*, 1996, **77**, 3865–3868.
- 47 P. E. Blöchl, *Phys. Rev. B: Condens. Matter Mater. Phys.*, 1994, **50**, 17953–17979.
- 48 H. J. Monkhorst and J. D. Pack, *Phys. Rev. B: Condens. Matter Mater. Phys.*, 1976, **13**, 5188–5192.
- 49 G. Henkelman, B. P. Uberuaga and H. Jónsson, *J. Chem. Phys.*, 2000, **113**, 9901–9904.
- 50 G. Henkelman and H. Jónsson, *J. Chem. Phys.*, 1999, **111**, 7010.
- 51 K. Momma and F. Izumi, *J. Appl. Crystallogr.*, 2011, **44**, 1272–1276.
- 52 B. D. Dunnington and J. Schmidt, *J. Chem. Theory Comput.*, 2012, **8**, 1902–1911.
- 53 F. Weigend and R. Ahlrichs, *Phys. Chem. Chem. Phys.*, 2005, **7**, 3297–3305.
- 54 B. D. Dunnington and J. Schmidt, *J. Catal.*, 2015, **324**, 50–58.
- 55 J. F. Weaver, *Chem. Rev.*, 2013, **113**, 4164–4215.
- 56 J. F. Weaver, C. Hakanoglu, A. Antony and A. Asthagiri, *Chem. Soc. Rev.*, 2014, **43**, 7536–7547.
- 57 C. Hall and R. N. Perutz, *Chem. Rev.*, 1996, **96**, 3125–3146.
- 58 J. Y. Saillard and R. Hoffmann, *J. Am. Chem. Soc.*, 1984, **106**, 2006–2026.
- 59 A. A. Latimer, H. Aljama, A. Kakekhani, J. S. Yoo, A. Kulkarni, C. Tsai, M. Garcia-Melchor, F. Abild-Pedersen and J. K. Nørskov, *Phys. Chem. Chem. Phys.*, 2017, **19**, 3575–3581.
- 60 R. A. van Santen, M. Neurock and S. G. Shetty, *Chem. Rev.*, 2009, **110**, 2005–2048.
- 61 H.-Y. Li, Y.-L. Guo, Y. Guo, G.-Z. Lu and P. Hu, *J. Chem. Phys.*, 2008, **128**, 051101.
- 62 J. F. Weaver, C. Hakanoglu, J. M. Hawkins and A. Asthagiri, *J. Chem. Phys.*, 2010, **132**, 024709.
- 63 S. Grimme, J. Antony, S. Ehrlich and H. Krieg, *J. Chem. Phys.*, 2010, **132**, 154104.
- 64 J. Sun, R. C. Remsing, Y. Zhang, Z. Sun, A. Ruzsinszky, H. Peng, Z. Yang, A. Paul, U. Waghmare and X. Wu, *Nat. Chem.*, 2016, **8**, 831–836.
- 65 A. V. Krukau, O. A. Vydrov, A. F. Izmaylov and G. E. Scuseria, *J. Chem. Phys.*, 2006, **125**, 224106.
- 66 J. Klimeš, D. R. Bowler and A. Michaelides, *J. Phys.: Condens. Matter*, 2010, **22**, 022201.
- 67 T. L. M. Pham, E. G. Leggesse and J. C. Jiang, *Catal. Sci. Technol.*, 2015, **5**, 4064–4071.
- 68 R. A. van Santen, M. Neurock and S. G. Shetty, *Chem. Rev.*, 2010, **110**, 2005–2048.